The Efficiency of Electron Acceleration during the Impulsive Phase of a Solar Flare

Eduard P. Kontar[1] , A. Gordon Emslie[2] , Galina G. Motorina[3] , and Brian R. Dennis[4]

[1] School of Physics & Astronomy, University of Glasgow, Scotland, UK
[2] Department of Physics and Astronomy, Western Kentucky University, Bowling Green, KY 42101, USA
[3] Astronomical Institute of the Czech Academy of Sciences, 251 65 Ondřejov, Czech Republic
[4] Solar Physics Laboratory, Code 671, Heliophysics Science Division, NASA Goddard Space Flight Center, Greenbelt, MD 20771, USA

Abstract

Solar flares are known to be prolific electron accelerators, yet identifying the mechanism(s) for such efficient electron acceleration in solar flare (and similar astrophysical settings) presents a major challenge. This is due in part to a lack of observational constraints related to conditions in the primary acceleration region itself. Accelerated electrons with energies above $\sim$20 keV are revealed by hard X-ray (HXR) bremsstrahlung emission, while accelerated electrons with even higher energies manifest themselves through radio gyrosynchrotron emission. Here, we show, for a well-observed flare on 2017 September 10, that a combination of RHESSI HXR and and the Solar Dynamics Observatory/Atmospheric Imaging Assembly (SDO/AIA) EUV observations provides a robust estimate of the fraction of the ambient electron population that is accelerated at a given time, with an upper limit of $\lesssim 10^{-2}$ on the number density of nonthermal ($\geqslant$20 keV) electrons, expressed as a fraction of the number density of ambient protons in the same volume. This upper limit is about 2 orders of magnitude lower than previously inferred from microwave observations of the same event. Our results strongly indicate that the fraction of accelerated electrons in the coronal region at any given time is relatively small but also that the overall duration of the HXR emission requires a steady resupply of electrons to the acceleration site. Simultaneous measurements of the instantaneous accelerated electron number density and the associated specific electron acceleration rate provide key constraints for a quantitative study of the mechanisms leading to electron acceleration in magnetic reconnection events.

1. Introduction

Spatially resolved hard X-ray (HXR) observations of solar flares reveal that electron acceleration likely occurs in magnetic reconnection outflow regions (see, e.g., Holman et al. 2011; Benz 2017, for reviews). Indeed, observations from the Ramaty High Energy Solar Spectroscopic Imager (RHESSI; Lin et al. 2002) observations have demonstrated (Sui & Holman 2003; Asai et al. 2007; Liu et al. 2008; Battaglia & Kontar 2013; Krucker & Battaglia 2014; Battaglia et al. 2019) the presence of faint sources of HXR emission above the tops of coronal loop structures as evidence for magnetic reconnection, as first noted by Masuda et al. (1994). These sources are consistent with regions where magnetic turbulence could provide sufficient power to accelerate electrons to the required energies (Kontar et al. 2017; Ruan et al. 2019; Chitta & Lazarian 2020; Stores et al. 2021). It is well known (e.g., Miller et al. 1997; Zharkova et al. 2011) that the total number of electrons accelerated during a large solar flare can exceed the total number of electrons in the coronal source region so that continuous resupply of the acceleration region (e.g., by a cospatial return current; Knight & Sturrock 1977; Emslie 1980; Zharkova & Syniavskii 1997; Alaoui & Holman 2017) is an essential ingredient of a viable electron acceleration model.

Spatially integrated bremsstrahlung HXR emission, produced during collisions of nonthermal electrons on ambient ions, provides direct diagnostics of the *total* electron acceleration rate $\dot{N}$ (s^{-1}) at energies above a specified energy (typically taken to be 20 keV). In such a "thick-target" calculation, the deduced electron acceleration rate is generally independent of the density structure of the flaring region, but the relationship between the accelerated electron distribution and the emitted HXR spectrum does depend on whether a cold (Brown 1971; Syrovatskii & Shmeleva 1972) or warm (Kontar et al. 2015) thick-target model is used. (The dependency of total acceleration rate arises through the difference in the energy loss term and transport through plasma (Kontar et al. 2019)—where the average energy of the ambient electrons is much smaller than the energy of the accelerated electrons—versus warm targets, where the energies of the accelerated and target particles can be comparable.) The inferred total electron acceleration rate depends strongly on the value of the low-energy spectral cutoff, which is difficult to determine from observations (e.g., Aschwanden et al. 2019, as a review).

In contrast with the spatially integrated case, the HXR flux spectrum from a given spatial subregion in the flare provides information on the density-weighted mean electron flux spectrum in that region. For this analysis, "thin-target" modeling (Brown et al. 2003) is used; this does not require any assumptions about the nature of the prevailing electron transport mechanism. This density weighting implies that bright HXR footpoints are conspicuously evident (e.g., Emslie et al. 2003; Kontar et al. 2008) because of the high density in the chromosphere, while strong coronal HXR sources are relatively rare (Holman et al. 2011) because the density is so low. Given the limited dynamic range of RHESSI and similar

instruments that employ indirect (Fourier-transform-based) imaging techniques, the problem of characterizing the HXR emission from low-density coronal acceleration regions is exacerbated by the presence of much brighter footpoint emission in the field of view.

Of considerable interest in understanding the nature of the process that accelerates particles to high energies are the ratios of the number densities (cm^{-3}) of nonthermal and thermal electrons (n_{nth} and n_{th}, respectively) to the total number density of background electrons, which, from considerations of charge neutrality, is equal to the number density of protons in the same region: $n_p = n_{th} + n_{nth}$ in the hydrogen plasma. The instantaneous fraction of accelerated electrons in the flaring corona has been previously discussed in the literature, but the results, methods, and the region that defines the "coronal source" and "above the loop top" differ somewhat and hence necessitates additional investigations. Krucker et al. (2010) reported $n_{nth}(>16\,\mathrm{keV})/n_p \simeq 0.1$, while Oka et al. (2013) reanalyzed the flare and deduced $n_{nth}(>20\,\mathrm{keV})/n_p \simeq 0.01$ (see their Equation (4)). Krucker & Battaglia (2014) analyzed a limb flare in the presence of bright footpoint emission and found $n_{nth}(>(10–15)\mathrm{keV})/n_p \simeq 1$ in the region above the coronal source, assuming a power-law spectrum with a sharp low-energy cutoff in the range from 10 to 15 keV. However, this high value was obtained using a Maxwellian+power-law fit to the HXR spectrum. Mean source electron spectra (Brown et al. 2003) in some coronal HXR sources have been found to be more consistent with a kappa distribution (Kašparová & Karlický 2009), which rolls over smoothly from a power law at high energies to a Maxwellian at low energies. Compared to fitting the thermal and nonthermal (power-law) parts of the spectrum separately, fitting the data with a kappa distribution generally results (as in Oka et al. 2013) in a significant reduction in the required electron flux near the rollover energy and hence a lower inferred value of n_{nth}. Indeed, Battaglia et al. (2015) demonstrate that using a kappa-distribution fit to RHESSI data, while also incorporating EUV emission line data to constrain the fit, results in a reduction in n_{nth} by a factor of up to ~30 compared with the commonly used power-law-only fit. Early in a flare, electron distributions in magnetic reconnection outflow regions could form a bulk thermal distribution with a relatively steep (e.g., power-law) nonthermal tail so that the electrons above, say, 20 keV represent only a small fraction of the total ambient population (Battaglia et al. 2019). However, the spectrum could change during the peak of the flare. Radio emission produced by gyrosynchrotron radiation of accelerated electrons with relatively high energies $\gtrsim 100\,\mathrm{keV}$ is also commonly observed in the flaring atmosphere (see Dulk & Marsh 1982; Nindos 2020, for reviews) and provides insight into the properties of electrons with energies higher than those that generate most of the HXR emission (e.g., White et al. 2011; Musset et al. 2018).

In this paper, we combine thin-target and thick-target modeling of RHESSI X-ray observations of a well-observed solar flare with contemporaneous EUV observations from the Solar Dynamics Observatory/Atmospheric Imaging Assembly (SDO/AIA; Lemen et al. 2012) in order to better constrain both the total number of accelerated electrons and the all-important ratio n_{nth}/n_p. The flare occurred on 2017 September 10 and revealed clear evidence (Chen et al. 2020) for a reconnection current sheet located above the flare loop top. Fleishman et al. (2022) have shown from Expanded Owens Valley Solar Array

(EOVSA; Gary et al. 2018) radio observations of this event that there was a relative dearth of thermal emission from an extended coronal volume but with considerable nonthermal emission from the same volume. They suggested that an inductive electric field of order 20 V cm^{-1} was generated by a magnetic field decay rate of order 5 G s^{-1} in a reconnection region of extent $\ell \simeq 4 \times 10^8$ cm and concluded that almost *all* of the electrons within that extended volume were accelerated to energies in excess of 20 keV, corresponding to $n_{nth}/n_p \simeq 1$ (and $n_{th}/n_p \simeq 0$). Our HXR and EUV observations conclusively demonstrate, however, that the instantaneous accelerated fraction n_{nth}/n_p is much less than unity, specifically $\lesssim 0.01$. Moreover, we argue that the accelerating electric fields are likely considerably smaller in magnitude than suggested by Fleishman et al. (2020) and Fleishman et al. (2022), indicative of a much smaller scale length $\ell \simeq 10^3$ cm associated with the reconnecting magnetic fields in the acceleration region.

2. X-Ray and EUV Observations

We consider the well-observed solar flare GOES X-class flare SOL2017-09-10T15:58, the GOES lightcurve of which is shown in Figure 1. This flare appeared at the western limb of the solar disk so that its vertical geometry can be well ascertained. The HXR emission evolved over tens of minutes, but we here focus on a narrow time interval near the peak of the impulsive phase, around 15:58 UT. The spatially integrated HXR spectrum at this time (Figure 2) shows both thermal and nonthermal components, with the spectrum dominated by nonthermal emission above about 30 keV.

The spatially integrated HXR spectrum can be used to infer the total number of accelerated electrons above a chosen reference energy, and dividing this by the volume of the HXR source (obtained from imaging spectroscopy data) leads to a measure of the accelerated electron number density n_{nth} (cm^{-3}). To quantify these relationships precisely, consider a region of volume V (cm^3), populated by accelerated electrons with number density spectrum $n(E)$ (electrons cm^{-3} keV^{-1}). The associated electron flux $F(E)$ (electrons cm^{-2} s^{-1} keV^{-1}) is $F(E) = n(E)\,v(E)$, where the (nonrelativistic) electron speed $v(E) = \sqrt{2E/m_e}$, m_e being the electron mass. This population of electrons produces a bremsstrahlung HXR spectrum $I(\epsilon)$ (photons cm^{-2} s^{-1} keV^{-1}) at a distance R from the emitting region given by Brown et al. (2003):

$$I(\epsilon) = \frac{1}{4\pi R^2} \int_\epsilon^\infty \langle n_p VF(E) \rangle\, \sigma(\epsilon, E)\, dE. \qquad (1)$$

Here $\sigma(\epsilon, E)$ is the bremsstrahlung cross section.[5] The quantity $\langle n_p VF(E) \rangle$ is the *mean source electron spectrum*, the volume integral of the local electron flux (differential in energy), weighted by the volume-averaged number density of target protons n_p, and $\langle \cdots \rangle$ emphasizes that the the quantity is a volume average. It is important to note that $\langle n_p VF(E) \rangle$ is directly determined from the observed HXR spectrum, requiring only knowledge of the bremsstrahlung cross section involved; no knowledge or assumptions regarding the source geometry or the physics governing the propagation of the accelerated electrons is required.

---

[5] See OSPEX software https://hesperia.gsfc.nasa.gov/rhessi3/software/spectroscopy/spectral-analysis-software/index.html.
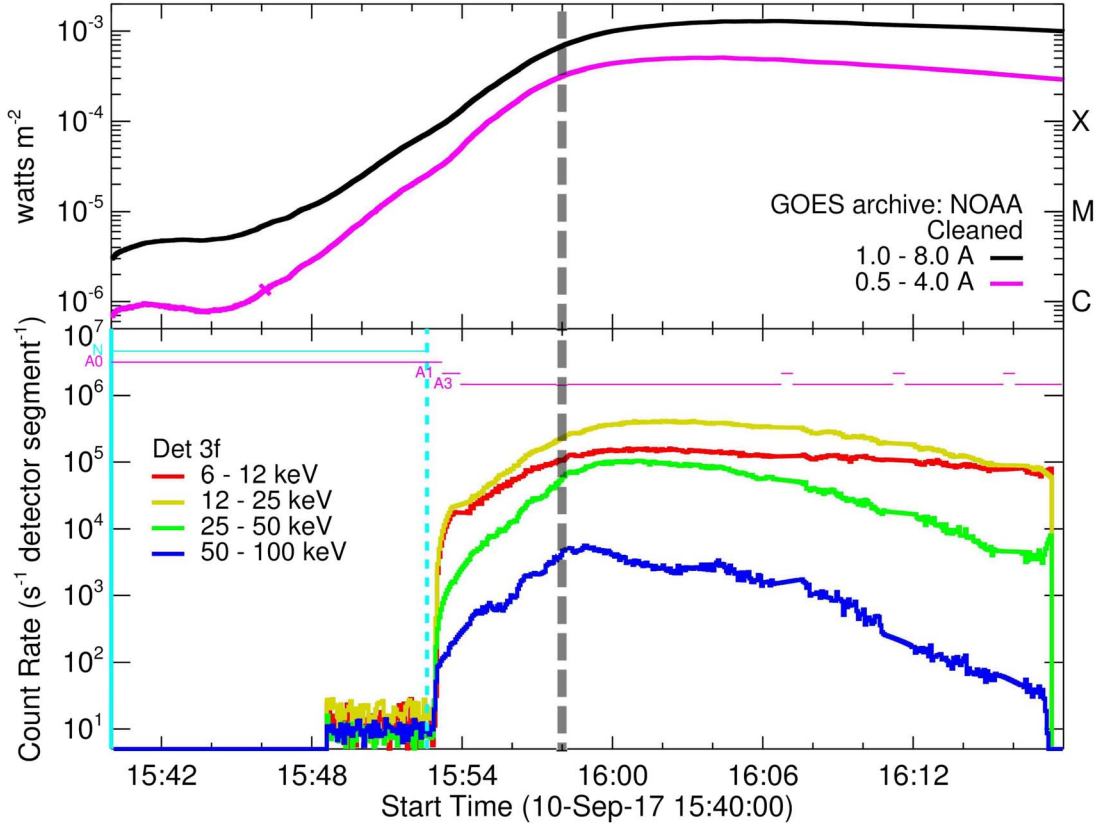
Figure 1. GOES and RHESSI X-ray lightcurves of the X8.2 flare on 2017 September 10 in the indicated energy ranges. Note that RHESSI data are only available from 15:52:30 UT at the start of the daytime part of the orbit until 16:17:30 UT on entry into the South Atlantic Anomaly. The horizontal purple lines indicate the times in the different attenuator states—A0, A1, and A3. The plotted count rates are shown for the front segment of detector #3 (3f), corrected to first order to the rates that would have been recorded in the A1 attenuator state, i.e., with only the thin attenuators in place. The dashed vertical line at 15:58 UT indicates the time interval of interest. Note that the periodic ripples in the lightcurves after about 16:06 UT are the result of uncorrected changes in the orientation of the instrument axis with respect to the spacecraft spin axis, caused by the attenuator motions (see Inglis et al. 2011).

Because the mean source electron spectrum corresponds to the instantaneous distribution of high-energy electrons in the coronal target, its form is obtained by a "thin-target" fit to the bremsstrahlung HXR spectrum. Figure 2 shows that the instantaneous spectrum of nonthermal electrons that best fits the HXR spectrum[6] for this event is well represented by a power law of the form

$$F(E) = (\delta - 1) \frac{\mathcal{F}_o}{E_o} \left(\frac{E}{E_o} \right)^{-\delta}, \qquad (2)$$

where E_o is a reference energy (e.g., a low-energy cutoff), $\mathcal{F}_o$ is the total electron flux (electrons $cm^{-2} s^{-1}$) above that energy, and δ is the power-law spectral index.

From this follows the accelerated number density spectrum (electrons $cm^{-3} keV^{-1}$)

$$n(E) = \frac{F(E)}{v(E)} = \sqrt{\frac{m_e}{2}} (\delta - 1) \mathcal{F}_o E_o^{\delta-1} E^{-\delta-1/2} \qquad (3)$$

so that the number density of nonthermal electrons n_{nth} (defined as the number of electrons per cm^3 that are accelerated to

energies above E_o) is

$$n_{\mathrm{nth}} = \int_{E_o}^{\infty} n(E) \, dE = \frac{(\delta - 1)}{\left(\delta - \frac{1}{2}\right)} \frac{\mathcal{F}_o}{v_o}, \qquad (4)$$

where $v_0 = \sqrt{2E_0/m_e} \simeq 8 \times 10^9$ cm s^{-1} for $E_0 = 20$ keV. The total mean source electron flux (electrons $cm^{-2} s^{-1}$ above energy E_o) may be written as the integral of the electron flux spectrum (Equation (2)) multiplied by the proton density and emitting volume so that

$$\langle n_p V \mathcal{F}_o \rangle = n_p \, V \int_{E_0}^{\infty} F(E) \, dE. \qquad (5)$$

Combining Equations (4) and (5), we find that

$$n_{\mathrm{nth}} \, n_p = \frac{(\delta - 1)}{\left(\delta - \frac{1}{2}\right)} \frac{\langle n_p V \mathcal{F}_o \rangle}{v_o \, V} = \frac{(\delta - 1)}{\left(\delta - \frac{1}{2}\right)} \sqrt{\frac{m_e}{2E_o}} \frac{\langle n_p V \mathcal{F}_o \rangle}{V}.$$

$$(6)$$

The observationally inferred value of $\langle n_p V \mathcal{F}_o \rangle$, coupled with estimates of the source volume V, thus straightforwardly constrains the product of the number of accelerated electrons n_{nth} and the mean number density of target protons n_p in the region under study.

Fleishman et al. (2022) have identified two "regions of interest" shown in Figure 3, region of interest (ROI)-1 (magenta line) and ROI-2 (black line). ROI-1 is the extended

---

[6] Thin-target fit using OSPEX: https://sohoftp.nascom.nasa.gov/solarsoft/packages/spex/doc/ospex_explanation.htm.
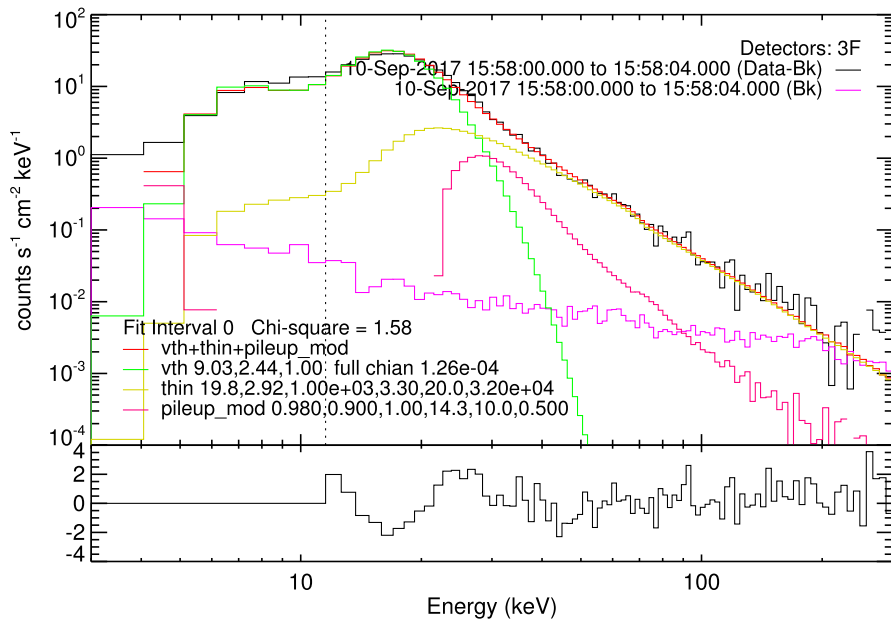
Figure 2. Spatially integrated HXR spectrum measured by detector #3, one of the four working RHESSI detectors near the peak of the flare, in a 4 s interval starting at 15:58 UT. The HXR spectrum is well fitted by a combination of thermal ("vth," green) and nonthermal ("thin," yellow) components. The "thin" function is used here for the nonthermal component assuming thin-target interactions of electrons with a power-law spectrum. The listed fit parameters are as follows: A(0) (here 19.8) is the value of $\langle n_p V \mathcal{F}_o \rangle$ (in units of 10^{55} electrons cm^{-2} s^{-1}) at energies above reference energy E_o, A(1) is the electron power-law index δ (here 2.92), and A(4) is the value of E_o (here 20 keV). The parameters A(2), A(3) and A(5) define the extended electron spectrum at energies above the range of interest in the present analysis, i.e., the upper limit ("break energy"; here 1000 keV) to this power law, the spectral index above this break energy (here 3.3), and the maximum energy for which the spectrum is computed (here 32 MeV). The thermal and nonthermal contributions are comparable at an X-ray energy $\epsilon \simeq 27$ keV. The total spectrum (red) also includes the pileup component (magenta curve) that peaks near 30 keV; the background spectrum is shown in magenta. The bottom panel shows residuals from the fit in units of the 1σ statistical uncertainties on the measured count rates at each energy.

curved elliptical region that outlines the volume in which they claim nearly 100% electron acceleration efficiency. This claim is based on EOVSA imaging spectroscopy analysis showing that ROI-1 has (1) a large nonthermal electron population, (2) a relative dearth of thermal electrons over an extended (4 minute) period of time, and (3) a rapid magnetic field decay (reported earlier by Fleishman et al. 2020) that leads to a large induced electric field capable of accelerating the entire ambient population in a very short time. For comparison, ROI-2 is identified as a region "of more typical flare plasma, outside the acceleration region."

X-ray imaging spectroscopy of this event can be made by analyzing RHESSI observations of the same flare. Various image reconstruction algorithms, described by Piana et al. (2022), can be used, such as Clean, MEM_NJIT, uv_smooth, and Vis_FwdFit. The X-ray image in Figure 3 was produced with the Clean method using observations over a 20 s interval centered at 15:58:00 UT. It reveals a source that we term ROI-0, with a FWHM area of 256 arcsec^2 and a centroid at a slightly lower altitude (some 15″) than ROI-1 and ROI-2. This image shows that the vast majority of the HXR emission at this time comes not from ROI-1 but rather from the compact ROI-0 source, the structure of which is rather poorly resolved by RHESSI.

X-ray spectra for each region of interest, produced using the RHESSI imaging spectroscopy technique described by Emslie et al. (2003), Battaglia & Benz (2006), Piana et al. (2007), Saint-Hilaire et al. (2008), and Jeffrey et al. (2014), are presented in Figure 4. These imaging spectroscopy results are somewhat limited for two reasons: (1) only four of the nine RHESSI germanium detectors (#1, #3, #6, and #8, with FWHM angular resolutions of 2″.3, 6″.8, 35″.3, and 106″,

respectively) were operational at this time, and (2) the count rates were sufficiently high to cause significant pulse pileup, where two or more low-energy photons arriving within a short time ($\sim$1 μ s) of each other are recorded as a single high-energy count. (One can see in Figure 2 a clear signature of pulse pileup at or below the 10%–20% level in the spectrum recorded by detector #3 near 30 keV; the effects of the pileup are weaker for other energies.) In general, at energies above the peak in the count-rate spectrum (here in the A3 attenuator state at $\sim$ 18 keV), pulse pileup tends to increase visibility amplitudes. This is especially true for the detectors with the coarser grids (#6 and #8) since the signals from these detectors have the greatest modulation amplitudes and the pileup effect is greater at the peaks of the modulation cycles than in the valleys. Detector #6 has the highest sensitivity of all the operating detectors so that the estimated source extent at the characteristic 35″ scale sampled by this detector is subject to an artificial increase; so the source could appear larger than the actual source extent, and hence the X-ray intensity in both ROI-1 and ROI-2 could be overestimated.

Performing spatial integrations over the three regions of interest (ROI-0 through ROI-2) results in the three HXR source spectra shown in Figure 4. Similar to the methodology of previous studies (e.g., Emslie et al. 2003), the HXR flux $I_o(\epsilon)$ from ROI-0 in each energy range is calculated by integrating over the FWHM area, while the spectra $I_1(\epsilon)$ and $I_2(\epsilon)$ from the weaker regions ROI-1 and ROI-2 are obtained by integrating the images over the entire areal extent of each respective region. We find that ROI-2 accounts for $\sim$30% of the total emission, while ROI-1 is rather faint, accounting for less than 10% of the total. Indeed, the HXR flux that appears to originate from ROI-1 in these reconstructed images is likely to be due
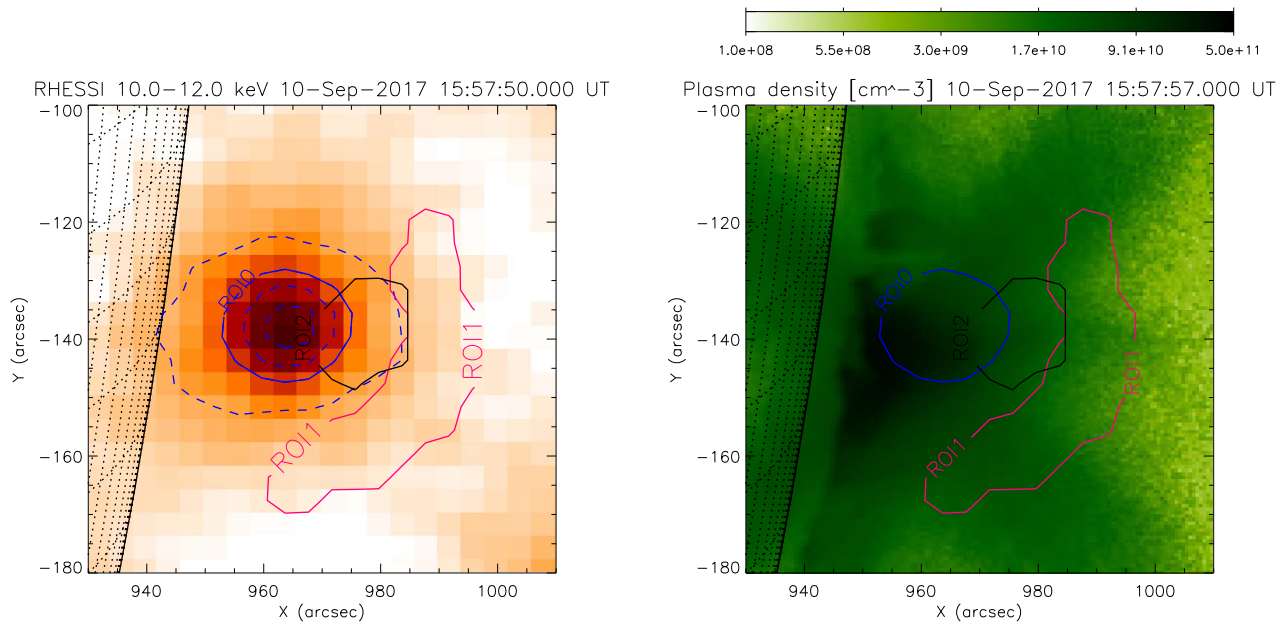
Figure 3. Left: clean RHESSI X-ray images using detectors #3 and #6 for the 20 s interval centered on 15:58 UT, with three regions of interest identified. The color-scale image represents thermal (10–12 keV) emission. The blue dashed lines are the contours at 20%, 70%, and 90% of the peak 50–100 keV nonthermal emission. The region of interest labeled ROI-0 is defined by the solid blue contour at the 50% level of the 50–100 keV image. Regions of interest ROI-1 and ROI-2 from Fleishman et al. (2022) are depicted by solid black and magenta boundary lines, respectively. Right: thermal plasma density map, also showing ROI-1 and ROI-2. This was constructed by applying a regularized differential emission measure algorithm (Hannah & Kontar 2012) to SDO/AIA data for the event in question, assuming the same line-of-sight distance of 8″ used by Fleishman et al. (2022).

mostly to a number of artifacts associated with pulse pileup, incomplete removal of side lobes from the intense compact source, and the limited number of spatial Fourier-transform components ("visibilities") measured with RHESSI (Hurford & Curtis 2002). Thus, the already-small inferred ROI-1 HXR fluxes $I_1(\epsilon)$ shown in Figure 4 represent *upper limits* to the actual HXR intensity from that region so that

$$\frac{I_{\text{ROI}-1}}{I_{\text{total}}} \leqslant 0.1.$$

Using the thin-target spectral fit to the spatially integrated HXR spectrum in Figure 2, the mean electron flux spectrum $\langle n_p V \mathcal{F}_o \rangle (E_o)$ for the entire flare is $\simeq 2 \times 10^{56}$ electrons cm^{-2} s^{-1} above reference energy $E_o = 20$ keV. Given the considerations of the previous paragraph, an upper limit for the mean source electron flux above 20 keV from ROI-1 is 10% of this value, i.e., $\langle n_p V \mathcal{F}_o \rangle_{\text{ROI}-1} \lesssim 2 \times 10^{55}$ electrons cm^{-2} s^{-1}. Using the cube of the source FWHM to estimate the volume of ROI-1 gives $V \simeq 1.6 \times 10^{27}$ cm^3, which agrees very well with the value $V = 1.7 \times 10^{27}$ cm^3 obtained by Fleishman et al. (2022) from radio observations. Substituting these values with $\delta = 2.92$ and $v_o = 8.4 \times 10^9$ cm s^{-1} in Equation (6) gives

$$n_{\text{nth}}\, n_p \lesssim 0.79 \times \frac{2 \times 10^{55}}{(8.4 \times 10^9)\,(1.6 \times 10^{27})}$$

$$\simeq 1.2 \times 10^{18}\ \text{cm}^{-6}. \qquad (7)$$

EUV images from SDO/AIA allow us to make an independent estimate of the density in ROI-1. Dividing the total emission measure $n_p^2 V$ of the EUV-emitting plasma in this region by the previously determined source volume, we find that the ambient proton density in this region (right panel of Figure 3) is $n_p \simeq 10^{10}$ cm^{-3}, i.e., consistent with densities commonly found in the preflare corona.

With this constraint in mind, we now consider the implications of Equation (7).

1. Fleishman et al. (2022) claim that all of the electrons in ROI-1 are accelerated, i.e., $n_{\text{nth}} \simeq 10^{10}$ cm^{-3} and moreover (their Figure 2c) that the number density of thermal electrons is depleted in ROI-1. However, due to the quasineutrality of the plasma, the proton density must be $n_p \simeq n_{\text{nth}}$; Equation (7) then shows that the number of nonthermal electrons cannot exceed 10^9 cm^{-3}. Extended data Figure 3 of Fleishman et al. (2022) shows a best-fit thermal plasma density of $10^{8.3}$ cm^{-3} (with an uncertainty of an order of magnitude or so) in their sample ROI-1 pixel. Extended data Figure 5(b) from the same Fleishman et al. (2022) work uses SDO/AIA data to conclude that the thermal number density n_{th} in ROI-2 has a value of order 10^{10} cm^{-3}. This value is consistent with our own estimates of the thermal density in that region (right panel of our Figure 3), and we would also note that our Figure 3 shows the SDO/AIA-inferred thermal densities in ROI-1 and ROI-2 to be comparable. The thermal density in the ROI-1 inferred from SDO/AIA data (our Figure 3) is some 2 orders of magnitude greater than the radio-observation-based estimates of the same quantity shown in Figure 2(c) of Fleishman et al. (2022).

2. If the average ambient (thermal) plasma density in ROI-1 is $n_p = 10^{10}$ cm^{-3}, as evidenced by the SDO/AIA observations (right panel of Figure 3), then $n_{\text{nth}}/n_p \simeq 0.012$, a value that is consistent with other estimates (e.g., Simões & Kontar 2013), kappa-like electron distribution in HXR coronal sources (Kašparová & Karlický 2009; Oka et al. 2013), and magnetic reconnection outflow regions (Battaglia et al. 2019).
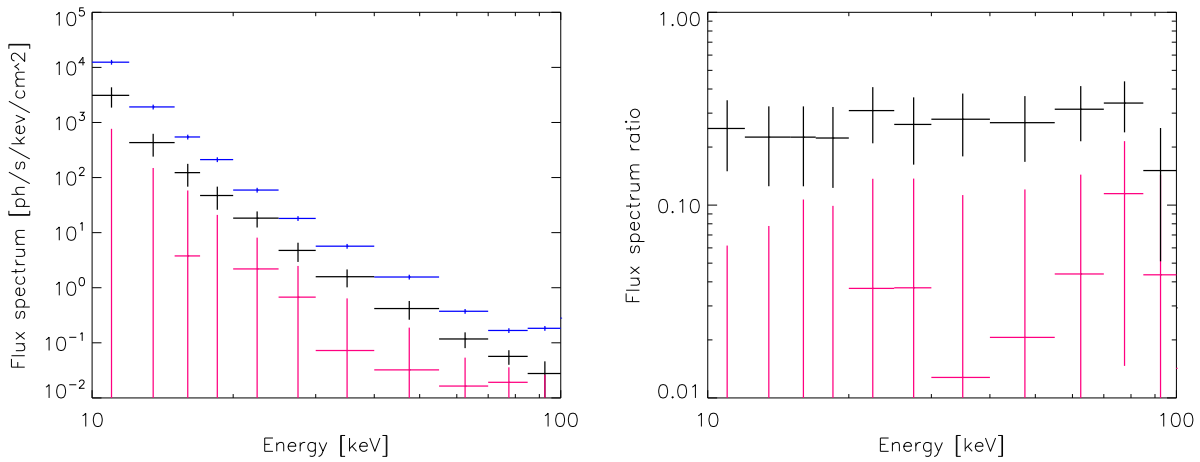
Figure 4. Left: HXR flux spectrum in the selected regions: the integrated emission is shown in blue, the emission from ROI-1 is shown in magenta, and the emission from ROI-2 is shown in black. Right: electron flux spectrum in ROI-1 (magenta) and ROI-2 (black), normalized by the image-integrated spectrum.

We believe that $n_{nth}/n_p \simeq 0.01$ in region ROI-1 is consistent with all the available observations of this flare and with reasonable expectations for the physical nature of ROI-1. The value of $n_{nth}(>20$ keV$)$ obtained from this reasoning can also be corroborated by appealing to thick-target (Brown 1971) modeling of the event. A thick-target fit to the spatially integrated HXR spectrum in Figure 2 gives an injected electron rate $\dot{N} \simeq 9 \times 10^{35}$ electrons s^{-1} above 20 keV. In a comparison of the electron rate at the loop top and at the footpoints, Simões & Kontar (2013) showed that the coronal $\dot{N}$ is on average $\sim 1.7 - 1.8$ times larger than the rate of electron precipitation toward the loop footpoints, with this difference resulting from some form of coronal trapping (e.g., turbulent scattering or magnetic mirroring). Applying this correction factor to the thick target $\dot{N}$ gives[7] a "loop top acceleration rate" $\dot{N}_{LT} = n_{nth} \, v_o \, A \simeq 5 \times 10^{35}$ electrons s^{-1}, corresponding to the rate at which electrons are injected from the loop top acceleration region into the surrounding target. Assuming that the cross-sectional area of the acceleration region is at least $A = 8'' \times 8'' \simeq 3.3 \times 10^{17}$ cm^2 and using $v_o \simeq 8.4 \times 10^9$ cm s^{-1} (corresponding to the low-energy cutoff electron energy $E_o = 20$ keV) gives $n_{nth} < 2 \times 10^8$ cm^{-3}, which is much lower than the ambient plasma density from SDO/AIA and gives $n_{nth}/n_p < 0.02$, consistent with the results from thin-target modeling of the ROI-1 region alone.

As a final self-consistency check, the nonthermal and thermal electron distribution maps reported by Fleishman et al. (2022) can be used in a thin-target model, *without any additional assumptions*, to produce simulated HXR maps. The simulated HXR emission map in the range 30–40 keV is shown in the right panel of Figure 5, together with the 50% contour of the HXR emission observed by RHESSI in the same energy range. This panel shows that the spatial distribution of simulated HXR emission based on the electron distribution maps of Fleishman et al. (2022) is not consistent with that observed by RHESSI. Specifically, the observed HXR flux

between 30–40 keV within the 50% contour level (Figure 5) is about 0.6 photons s^{-1} arcsec^{-2} cm^{-2}, but the nonthermal and thermal electron densities inferred by Fleishman et al. (2022) would predict a significantly higher HXR count rate in many pixels of ROI-1. In fact, the simulated flux for some $2'' \times 2''$ pixels exceeds the observed emission from the entire flare volume.

We further note that the radio spectrum analysis by Fleishman et al. (2022) is performed over $2''$ pixels. This scale is well below the EOVSA beam resolution of $(45 - 5)''$ for the $(2 - 18)$ GHz range so that their nonthermal electron maps must be interpreted with a considerable degree of caution. The required angular resolution ($1''$ at 15 GHz) with better sensitivity and unprecedented u–v coverage could, however, be achieved by the Square Kilometre Array that is under construction (Nindos et al. 2019), and we encourage such observations,[8] ideally in concert with simultaneous HXR imaging spectroscopy measurements (e.g., from the STIX instrument on Solar Orbiter).

3. Summary and Discussion

The results of the previous section, based on RHESSI HXR and SDO/AIA observations of the 2017 September 10 flare, show a discrepancy with the results presented by Fleishman et al. (2020). Our analysis indicates that the ratio of nonthermal electrons to ambient electrons in ROI-1 at a time near the peak of the X-ray emission is $n_{nth}/n_p \simeq 0.01 - 0.02$, while the analysis by Fleishman et al. (2022) using radio observations alone suggests that $n_{nth}/n_p \simeq 1$. In light of these widely discrepant values of n_{nth}/n_p (or, equivalently, the significant excess of HXR emission predicted by the model of Fleishman et al. (2022), compared with the actual RHESSI observations of the same event—Figure 5), it is worthwhile to revisit the arguments of Fleishman et al. (2020) regarding the values of the physical parameters that characterize the primary reconnection process.

First, we remark that the mean kinetic energy per electron $\langle E \rangle = (1/n_{nth}) \int_{E_o}^{\infty} E \, n(E) \, dE$ inferred by Fleishman et al. (2022) for ROI-1 corresponds to ~ 25 keV or $\langle E \rangle / k_B \simeq 250$ megakelvin (MK), in a region (Figure 5) where the thermal

---

[7] It should be noted that the event in question was a west limb event, with no obvious footpoint sources visible. It is possible that the coronal density is high enough that the corona acts as a thick target (Veronig & Brown 2004), effectively stopping the electrons before they reach the chromosphere. However, if the footpoint sources were indeed occulted by the solar photosphere, the observed HXR intensity does not represent the entire HXR emission, and thus the precipitation rate $\dot{N}_{LT}$, and hence the inferred value of n_{nth}, are higher than those obtained from the observed HXR flux.

[8] The Frequency Agile Solar Radiotelescope, which is currently under development (Gary et al. 2022), could also be very useful in this regard.
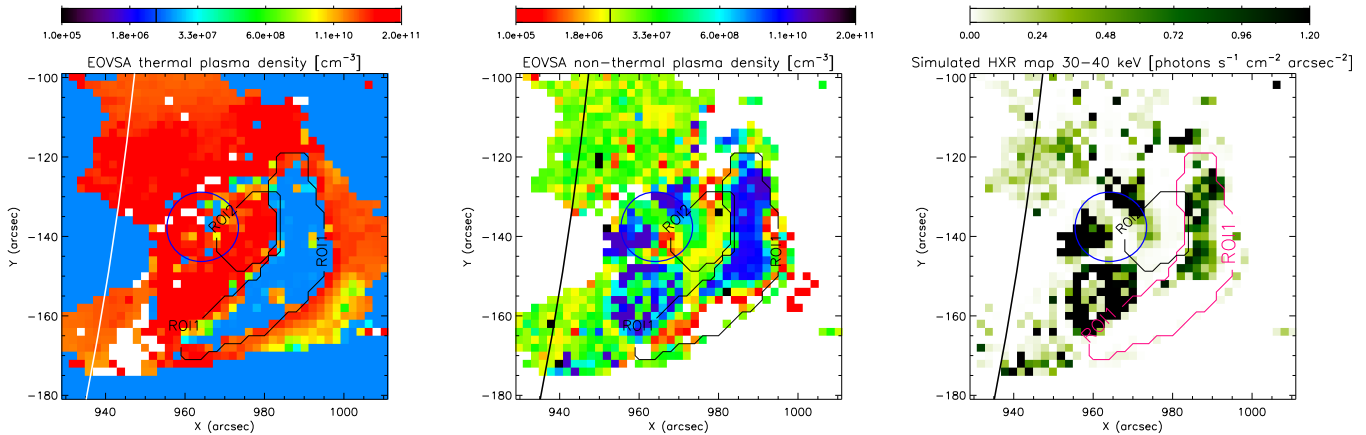
Figure 5. Thermal plasma (left panel) and nonthermal (above 20 keV, center panel) electron number densities as inferred by Fleishman et al. (2022). The right panel shows the corresponding simulated HXR emission, while the blue contour shows the 50% level (0.6 photons cm^{-2} s^{-1} arcsec^{-2}) obtained from RHESSI imaging spectroscopy observations in the 30–40 keV range over the same time interval used for Figure 2.

electron density is claimed to be negligible. This vastly exceeds commonly accepted values of $20 - 30$ MK for most flare bulk plasma components (see, e.g., Doschek et al. 1979; Dennis 1988; Holman et al. 2011; Aschwanden et al. 2017; Benz 2017, for reviews) and even exceeds that of the so-called "superhot" component at a temperature of 30–50 MK that has been inferred in some events (Lin et al. 1985; Phillips 1996; Caspi et al. 2014). The bulk energization of a volume of solar plasma to such high equivalent temperatures therefore represents an unprecedented situation.

Second, Fleishman et al. (2022) use Faraday's law $\nabla \times \mathcal{E} = (1/c) \, \partial B / \partial t$ and write $\nabla \times \mathcal{E} \simeq \mathcal{E}/\ell$, where ℓ is a characteristic scale length associated with the gradient in the reconnecting magnetic field region. This gives[9] $\mathcal{E} \simeq (300 \, \ell/c) \, \partial B / \partial t = (\ell/10^8) \, \partial B / \partial t$ V cm^{-1}. Using a value $\partial B / \partial t \simeq 5$ G s^{-1}, based on observations reported by Fleishman et al. (2020), and further estimating that $\ell = 3.65 \times 10^8$ cm (corresponding to $5''$ on the solar disk), Fleishman et al. (2022) obtain $\mathcal{E} \simeq 20$ V cm^{-1}, more than 5 orders of magnitude greater than the Dreicer (1959) field $\mathcal{E}_D \simeq 4 \times 10^{-4} \, (n/10^{10} \, \text{cm}^{-3}) \, (10^6 \, \text{K}/T) \simeq 1.3 \times 10^{-4}$ V cm^{-1} (for a density $n = 10^{10}$ cm^{-3} and a temperature $T = 3 \times 10^6$ K). Under the influence of such a large electric field, all of the electrons in the ambient Maxwellian distribution would be accelerated, and they would reach an energy of 20 keV over a very short distance $L \simeq 10^3$ cm, some 5 orders of magnitude less than the assumed reconnection scale ℓ. This is not consistent with the claim of Fleishman et al. (2022) that "this strong super-Dreicer field must be present over a substantial portion of ROI-1." Such a value of L also corresponds to an acceleration time $L/v \simeq 10^{-7}$ s and thus, with an accelerated fraction of unity, to a *specific acceleration rate* (fraction of electrons accelerated to 20 keV per unit time; Emslie et al. 2008; Guo et al. 2012, 2013) $\eta \, (20 \, \text{keV}) \simeq 1/10^{-7} = 10^7$ s^{-1}, 9 orders of magnitude greater than previously inferred for other flares (Guo et al. 2013).

Significant runaway acceleration of the electrons in the ambient Maxwellian will, however, occur for electric field strengths $\mathcal{E}$ that are merely of order of the Dreicer field, much lower than the field strength claimed by Fleishman et al. (2022). Furthermore, once this runaway acceleration

commences, the fundamental electrodynamic properties in the acceleration region (including the replacement of accelerated particles by a cospatial return current) will change sufficiently that further buildup of the electric field is not necessary and, indeed, is unlikely. Using an illustrative reconnection scale length value $\ell = 10^3$ cm and the same 5 G s^{-1} rate of change of magnetic field inferred by Fleishman et al. (2020), the resulting induced electric field $\mathcal{E} \simeq 5 \times 10^{-8} \, \ell \simeq 5 \times 10^{-5}$ V cm^{-1}, approximately one-third of the Dreicer field. Such a field will cause runaway acceleration of electrons with $v \gtrsim v_{\text{crit}} = \sqrt{\mathcal{E}_D/\mathcal{E}} \, v_{\text{th}} \simeq \sqrt{3} \, v_{\text{th}}$ representing a fraction $0.5 \times \text{erfc}(\sqrt{3}/\sqrt{2}) \simeq 5\%$ of the ambient Maxwellian distribution. However, it is very likely that the acceleration region is highly inhomogeneous so that the required electron energies are reached through a more stochastic process involving a succession of smaller impulses acting in different directions and with different efficiencies so that electrons are accelerated through a Fermi acceleration process (e.g., Miller et al. 1997; Bian et al. 2012; Zank et al. 2015; Gordovskyy et al. 2020; Arnold et al. 2021) rather than as the result of a single large-scale unidirectional acceleration event.

With 5% of the electron population undergoing runaway acceleration to deka-keV energies at any given time and a collisional repopulation of the tail on a timescale of 0.5 s, the *instantaneous* number density of accelerated electrons, n_{nth}, corresponding to the number density of electrons in the high-energy runaway tail of the distribution, is a relatively small fraction of the ambient number density n_p. Further, the associated value of the specific acceleration rate is $\eta \, (20 \, \text{keV}) \simeq 0.05/0.5 = 0.1$ s^{-1}, consistent with the RHESSI and SDO/AIA observations of Section 2 and comparable to the specific acceleration rates inferred previously using different methods (e.g., Guo et al. 2013). In contrast, a much larger overall population of electrons is successively accelerated over significantly longer timescales. For an ambient density $n_p \simeq 10^{10}$ cm^{-3} and a source volume $V \simeq 10^{27}$ cm^3, the total number of available electrons is $\simeq 10^{37}$ so that the electron acceleration rate of 9×10^{35} s^{-1} inferred from thick-target modeling of the event (Section 2) corresponds to an acceleration of all the electrons in the corona in ~ 10 s, shorter than the duration of the HXR burst. This constitutes the well-known "number problem" (e.g., Brown 1971) that requires a continual replenishment of the acceleration region, e.g., by a cospatial return current carried by ambient thermal electrons

---

[9] The factor 300 converts the centimetre–gram–second statvolt units into volts.

(Knight & Sturrock [1977](#); Emslie [1980](#); Alaoui & Holman [2017](#)).

The dramatically different values for (n_{nth}/n_p) from $\simeq 0.01$ to $\simeq 1$, clearly present us with a dilemma. How are such disparate results to be reconciled? One possibility lies in the fact that the emitted microwave flux is rather insensitive to the value of the low-energy cutoff energy E_o (see Figure 1 in Holman [2003](#)). Further, extended data Figure 3 of Fleishman et al. ([2022](#)) claims a relatively high spectral index $\delta \simeq 5-6$ for a "typical" pixel in ROI-1, much higher than the value $\delta \simeq 3$ obtained from the total spatially integrated HXR spectrum (Figure [2](#)). This indicates (probably similarly to Chen et al. [2021](#)) that such a high value of δ is not applicable to the deka-keV regime from which most of the contribution to n_{nth} arises. Such a flattening of the electron spectrum at lower energies would reduce the value of n_{nth} from that claimed by Fleishman et al. ([2022](#)). Indeed, since the total number of accelerated electrons ($\int_{E_o}^{\infty} E^{-\delta-1/2} dE \propto E_o^{1/2-\delta}$; Equation ([3](#))) depends rather sensitively on the the values of both E_o and δ, it is possible that a much lower value of n_{nth}, comparable with that deduced from HXR and EUV observations, is also consistent with the observed microwave emission. Interestingly, the self-consistent simulations of electron acceleration during magnetic reconnection in a macroscale system (Arnold et al. [2021](#)), as well as spatially extended turbulent electron acceleration (Stores et al. [2023](#)), also suggest that the instantaneous number density of nonthermal electrons remains small.

ORCID iDs

Eduard P. Kontar ● https://orcid.org/0000-0002-8078-0902
A. Gordon Emslie ● https://orcid.org/0000-0001-8720-0723
Galina G. Motorina ● https://orcid.org/0000-0001-7856-084X
Brian R. Dennis ● https://orcid.org/0000-0001-8585-2349

References

Alaoui, M., & Holman, G. D. 2017, ApJ, 851, 78
Arnold, H., Drake, J. F., Swisdak, M., et al. 2021, PhRvL, 126, 135101
Asai, A., Nakajima, H., Oka, M., Nishida, K., & Tanaka, Y. T. 2007, AdSpR, 39, 1398
Aschwanden, M. J., Caspi, A., Cohen, C. M. S., et al. 2017, ApJ, 836, 17
Aschwanden, M. J., Kontar, E. P., & Jeffrey, N. L. S. 2019, ApJ, 881, 1
Battaglia, M., & Benz, A. O. 2006, A&A, 456, 751
Battaglia, M., & Kontar, E. P. 2013, ApJ, 779, 107
Battaglia, M., Kontar, E. P., & Motorina, G. 2019, ApJ, 872, 204

Battaglia, M., Motorina, G., & Kontar, E. P. 2015, ApJ, 815, 73
Benz, A. O. 2017, LRSP, 14, 2
Bian, N., Emslie, A. G., & Kontar, E. P. 2012, ApJ, 754, 103
Brown, J. C. 1971, SoPh, 18, 489
Brown, J. C., Emslie, A. G., & Kontar, E. P. 2003, ApJL, 595, L115
Caspi, A., Krucker, S., & Lin, R. P. 2014, ApJ, 781, 43
Chen, B., Battaglia, M., Krucker, S., Reeves, K. K., & Glesener, L. 2021, ApJL, 908, L55
Chen, B., Shen, C., Gary, D. E., et al. 2020, NatAs, 4, 1140
Chitta, L. P., & Lazarian, A. 2020, ApJL, 890, L2
Dennis, B. R. 1988, SoPh, 118, 49
Doschek, G. A., Kreplin, R. W., & Feldman, U. 1979, ApJL, 233, L157
Dreicer, H. 1959, PhRv, 115, 238
Dulk, G. A., & Marsh, K. A. 1982, ApJ, 259, 350
Emslie, A. G. 1980, ApJ, 235, 1055
Emslie, A. G., Hurford, G. J., Kontar, E. P., et al. 2008, in AIP Conf. Ser. 1039, ed. G. Li et al. (Melville, NY: AIP), 3
Emslie, A. G., Kontar, E. P., Krucker, S., & Lin, R. P. 2003, ApJL, 595, L107
Fleishman, G. D., Gary, D. E., Chen, B., et al. 2020, Sci, 367, 278
Fleishman, G. D., Nita, G. M., Chen, B., Yu, S., & Gary, D. E. 2022, Natur, 606, 674
Gary, D. E., Chen, B., Dennis, B. R., et al. 2018, ApJ, 863, 83
Gary, D. E., Chen, B., Drake, J. F., et al. 2022, arXiv:2210.10827
Gordovskyy, M., Browning, P. K., Inoue, S., et al. 2020, ApJ, 902, 147
Guo, J., Emslie, A. G., Massone, A. M., & Piana, M. 2012, ApJ, 755, 32
Guo, J., Emslie, A. G., & Piana, M. 2013, ApJ, 766, 28
Hannah, I. G., & Kontar, E. P. 2012, A&A, 539, A146
Holman, G. D. 2003, ApJ, 586, 606
Holman, G. D., Aschwanden, M. J., Aurass, H., et al. 2011, SSRv, 159, 107
Hurford, G. J., & Curtis, D. W. 2002, SoPh, 210, 101
Inglis, A. R., Zimovets, I. V., Dennis, B. R., et al. 2011, A&A, 530, A47
Jeffrey, N. L. S., Kontar, E. P., Bian, N. H., & Emslie, A. G. 2014, ApJ, 787, 86
Kašparová, J., & Karlický, M. 2009, A&A, 497, L13
Knight, J. W., & Sturrock, P. A. 1977, ApJ, 218, 306
Kontar, E. P., Hannah, I. G., & MacKinnon, A. L. 2008, A&A, 489, L57
Kontar, E. P., Jeffrey, N. L. S., & Emslie, A. G. 2019, ApJ, 871, 225
Kontar, E. P., Jeffrey, N. L. S., Emslie, A. G., & Bian, N. H. 2015, ApJ, 809, 35
Kontar, E. P., Perez, J. E., Harra, L. K., et al. 2017, PhRvL, 118, 155101
Krucker, S., & Battaglia, M. 2014, ApJ, 780, 107
Krucker, S., Hudson, H. S., Glesener, L., et al. 2010, ApJ, 714, 1108
Lemen, J. R., Title, A. M., Akin, D. J., et al. 2012, SoPh, 275, 17
Lin, H. A., Lin, R. P., & Kane, S. R. 1985, SoPh, 99, 263
Lin, R. P., Dennis, B. R., Hurford, G. J., et al. 2002, SoPh, 210, 3
Liu, W., Petrosian, V., Dennis, B. R., & Jiang, Y. W. 2008, ApJ, 676, 704
Masuda, S., Kosugi, T., Hara, H., Tsuneta, S., & Ogawara, Y. 1994, Natur, 371, 495
Miller, J. A., Cargill, P. J., Emslie, A. G., et al. 1997, JGR, 102, 14631
Musset, S., Kontar, E. P., & Vilmer, N. 2018, A&A, 610, A6
Nindos, A. 2020, FrASS, 7, 57
Nindos, A., Kontar, E. P., & Oberoi, D. 2019, AdSpR, 63, 1404
Oka, M., Ishikawa, S., Saint-Hilaire, P., Krucker, S., & Lin, R. P. 2013, ApJ, 764, 6
Phillips, A. T. 1996, AdSpR, 17, 39
Piana, M., Emslie, A. G., Massone, A. M., & Dennis, B. R. 2022, Hard X-ray Imaging of Solar Flares (Berlin: Springer-Verlag),
Piana, M., Massone, A. M., Hurford, G. J., et al. 2007, ApJ, 665, 846
Ruan, W., Xia, C., & Keppens, R. 2019, ApJL, 877, L11
Saint-Hilaire, P., Krucker, S., & Lin, R. P. 2008, SoPh, 250, 53
Simões, P. J. A., & Kontar, E. P. 2013, A&A, 551, A135
Stores, M., Jeffrey, N. L. S., & Kontar, E. P. 2021, ApJ, 923, 40
Stores, M., Jeffrey, N. L. S., & McLaughlin, J. A. 2023, ApJ, 946, 53
Sui, L., & Holman, G. D. 2003, ApJL, 596, L251
Syrovatskii, S. I., & Shmeleva, O. P. 1972, SvA, 16, 273
Veronig, A. M., & Brown, J. C. 2004, ApJL, 603, L117
White, S. M., Benz, A. O., Christe, S., et al. 2011, SSRv, 159, 225
Zank, G. P., Hunana, P., Mostafavi, P., et al. 2015, ApJ, 814, 137
Zharkova, V. V., Arzner, K., Benz, A. O., et al. 2011, SSRv, 159, 357
Zharkova, V. V., & Syniavskii, D. V. 1997, A&A, 320, L13

---

[10] https://hesperia.gsfc.nasa.gov/rhessi3/